J. Electroanal. Chem., 360 (1993) 101–118
Elsevier Sequoia S.A., Lausanne
JEC 02817

Impedance studies of porous lanthanum-phosphate-bonded nickel electrodes in concentrated sodium hydroxide solution

Przemyslaw Los *, Andrzej Lasia and Hugues Ménard
Département de Chimie, Université de Sherbrooke, Québec J1K 2R1 (Canada)

Louis Brossard
Institut de recherche d'Hydro-Québec, Varennes, Québec J3X 1S1 (Canada)

(Received 30 November 1992; in revised form 8 March 1993)

Abstract

The hydrogen evolution reaction (HER) was investigated on a lanthanum-phosphate-bonded nickel (LPBN) powder electrode in 30 wt.% NaOH at 70°C using ac impedance and steady-state polarization techniques. Circuits containing one or two constant-phase elements (CPEs) in parallel with a resistance and corresponding to fractal and porous electrode models were tested in order to interpret the ac impedance data. The experimental impedance spectra were well described by the porous electrode model and the circuit containing two CPEs. The results obtained from the ac impedance and steady-state measurements allowed the mechanism and kinetics of the HER to be evaluated. Comparison of these parameters with those obtained on the polycrystalline nickel electrode in 1 M alkaline solution at 25°C indicates that an increase in activity is principally due to an increase in the real surface area.

INTRODUCTION

Water electrolysis is one of several methods of producing hydrogen. Nickel is the most commonly used commercial anodic and cathodic material, but great efforts are being made to find new active electrodes [1–19]. A new method of binding nickel powder with an inorganic lanthanum phosphate polymer has been developed in this laboratory and employed to obtain highly electroactive and

* On leave from Department of Pharmacy, Medical University, 50-139 Wroclaw (Poland).

0022-0728/93/$06.00 © 1993 – Elsevier Sequoia S.A. All rights reserved

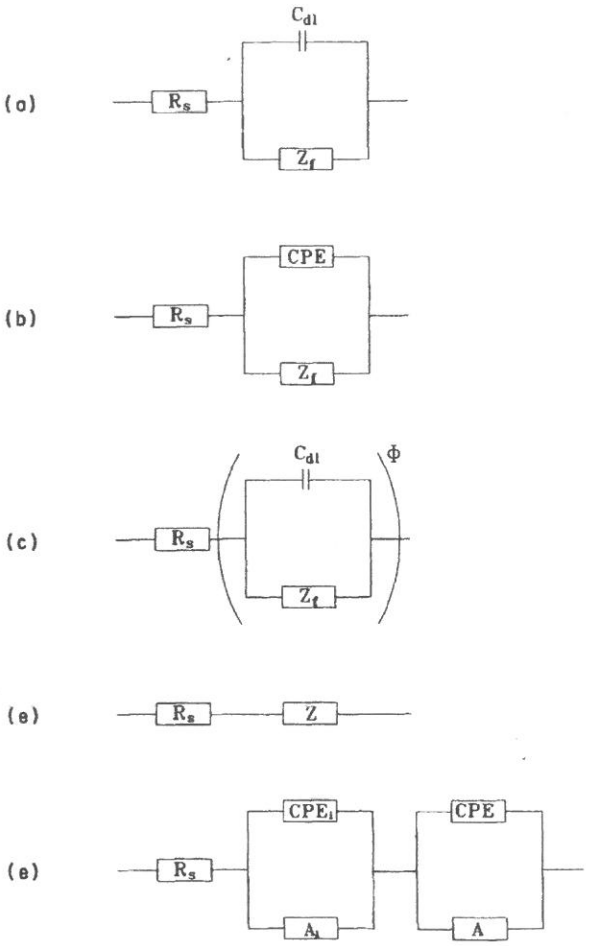

Fig. 1. Equivalent circuits used for the HER: (a) Randles equivalent model; (b) CPE model; (c) fractal model; (d) porous electrode model; (e) two constant-phase element (CPE1-CPE) model.

For the faradaic reaction on liquid (ideally smooth) electrodes, the equivalent circuit consists of the solution resistance R_s in series with the parallel double-layer capacitance C_{dl} and the faradaic impedance Z_f (Fig. 1(a)). According to Harrington and Conway [31], the faradaic impedance can be represented by

$$Y_f = 1/Z_f = A + B/(j\omega + C) \tag{7}$$

where

$$A = -F(\partial r_0/\partial \eta)_\Theta \tag{8}$$

$$B = -(F^2/\sigma_1)(\partial r_0/\partial \Theta)_\eta (\partial r_1/\partial \eta)_\Theta \tag{9}$$

$$C = -(F/\sigma_1)(\partial r_1/\partial \Theta)_\eta \tag{10}$$

where $r_0 = \vartheta_1 + \vartheta_2$, $r_1 = \vartheta_1 - \vartheta_2 - 2\vartheta_3$ and σ_1 is the charge necessary for monolayer coverage by the adsorbed atomic hydrogen. However, for solid electrodes, even in the absence of the faradaic reaction, a simple circuit containing R_s and C_{dl} in series cannot be considered to interpret measured impedances since the time constants are dispersed.

In previous studies of LPBN electrodes in 1 M alkaline solutions at 25°C, a successful fit of ac measurements was obtained using a CPE model (Fig. 1(b)) [16,17,37] in which the double-layer capacity is replaced by the CPE impedance defined by

$$Z_{CPE} = 1/\left[T(j\omega)^{\phi}\right] \tag{11}$$

where T is a constant which may depend on the electrode potential. In this case, the electrode impedance Z_{el} is given by

$$1/Z_{el} = Y_{el} = T(j\omega)^{\phi} + 1/Z_f \tag{12}$$

Brug et al. [37] have suggested that when the distributed capacitance is coupled with the charge-transfer resistance, the double-layer capacitance can be evaluated from the following equation:

$$T = (C_{dl})^{\phi}\left[(R_s)^{-1} + (R_{ct})^{-1}\right]^{(1-\phi)} \tag{13}$$

where $R_{ct} = 1/A$ is the charge-transfer resistance. Experimentally, the CPE behavior is expressed by the clockwise rotation of the complex plane plot obtained for a smooth electrode through an angle of $90°(1 - \phi)$.

In the fractal model (Fig. 1(c)) [38–40] a frequency dispersion of the double-layer capacitance and charge-transfer resistance yields the following expression for the electrode admittance:

$$Y_{el} = b(j\omega C + 1/R_{ct})^{\phi} \tag{14}$$

where b is a parameter depending on the solution resistance and electrode geometry and ϕ is the CPE exponent. As shown by de Levie [39], eqn. (14) is applicable only in the absence of a net faradaic current. Since a priori determination of parameter b is difficult, the fractal model does not allow the double-layer capacity or the charge-transfer resistance to be determined. The only experimentally accessible parameters are the real parameters multiplied by $b^{1/\phi}$, i.e. $C_{dl,exp} = C_{dl}b^{1/\phi}$ or $A_{exp} = Ab^{1/\phi}$ [14,41,42]. It should be noted that the fractal model describes the ideally smooth interface for $\phi = 1$ and de Levie's porous electrodes for $\phi = 0.5$.

A model of deep cylindrical pores was proposed by de Levie [43] (Fig. 1(d)) and found that the impedance is given by the equation

$$Z = R_s + Z_p/n \tag{15}$$

where n is the number of pores and the impedance of a single cylindrical pore is given by

$$Z_p = (1/\pi r)(\rho Z_0/2r)^{1/2} \coth\left(2\rho l^2/rZ_0\right)^{1/2} \tag{16}$$

In eqn. (16), Z_0 stands for the specific impedance per unit area of the flat surface of a cylindrical pore, r and l are the pore radius and pore length respectively, and ρ is the specific resistance of the solution. For a pure charge-transfer-controlled process, Z_0 can be described by the parallel connection of the charge-transfer resistance R_{ct} and the double-layer capacitance C_{dl}, i.e. $Z_0 = (1/R_{ct} + j\omega C_{dl})^{-1}$. It is well known [27,43–47], that the behavior of a porous electrode depends on the value of the ratio l/λ, where λ is the penetration depth of the ac signal and equals $(rZ_0/2\rho)^{1/2}$. de Levie [43] reported that for $l \geqslant 3\lambda$ the pore behaves as semi-infinite and for $l \leqslant 0.2\lambda$ it responds like a flat electrode. A similar conclusion can be drawn using the following equations [20] for the dimensionless electrode admittance Λ and for Z:

$$\Lambda = (1/a)(1/R_{ct} + j\omega C_{dl}) = 1/\mathscr{A}_p + j\omega\mathscr{B}_p \tag{17}$$

$$Z = R_s + \left(R_{\Omega,p}/\Lambda^{1/2}\right)\left[\coth(\Lambda^{1/2})\right] \tag{18}$$

where $R_{\Omega,p} = \rho l/n\pi r^2$ is the electrolyte resistance along the pore axis, $\mathscr{A}_p = aR_{ct}$, $\mathscr{B}_p = C_{dl}/a$ and $a = r/2\rho l^2$. The complex plane plot corresponding to this equation is shown in Fig. 2, curve a. This curve is a straight line at high frequencies and a semicircle at low frequencies. It is easy to show that the general equation (18) can be simplified to two limiting cases. First, when $\lambda \gg l$, $\Lambda^{1/2} = l/\lambda \to 0$, coth $\Lambda^{1/2} \to 1/\Lambda^{1/2}$:

$$\begin{aligned} Z &= R_s + R_{\Omega,p}/\Lambda = R_s + R_{\Omega,p}a(1/R_{ct} + j\omega C_{dl})^{-1} \\ &= R_s + (1/s)(1/R_{ct} + j\omega C_{dl})^{-1} \end{aligned} \tag{19}$$

where $s = 2n\pi rl$ is the total surface area of the pore walls. In this case, the complex impedance plot is represented by a semicircle (Fig. 2, curve b) with diameter equal to R_{ct}/s. In the other limiting case $\lambda \ll l$, $\Lambda \to \infty$, coth $\Lambda^{1/2} \to 1$ (coth$(x) = 1$ for $x > 3$) and eqn. (18) simplifies to

$$Z = R_s + R_{\Omega,p}/\Lambda^{1/2} = R_s + R_{\Omega,p}a^{1/2}(1/R_{ct} + j\omega C_{dl})^{-1/2} \tag{20}$$

or

$$Z = R_s + \left\{\rho^{1/2}/\left[(2r^3)^{1/2}n\pi\right]\right\}(1/R_{ct} + j\omega C_{dl})^{-1/2} \tag{20a}$$

As a result the complex plane plot is a deformed semicircle (Fig. 2, curve c). It should be added that eqn. (20) is formally identical with that for the fractal model for $\phi = 0.5$. The value of Z' for $\omega \to 0$ is equal to $R_s + R_{\Omega,p}(aR_{ct})^{1/2}$ or $R_s + R_{\Omega,p}(\mathscr{A}_p)^{1/2}$. It is worth noting that, in general, the low frequency value $Z'(\omega \to 0)$ is greater than $Z'(\omega \to 0) = R_s + R_{ct}/s$ obtained in the limiting case when $\Lambda \to 0$.

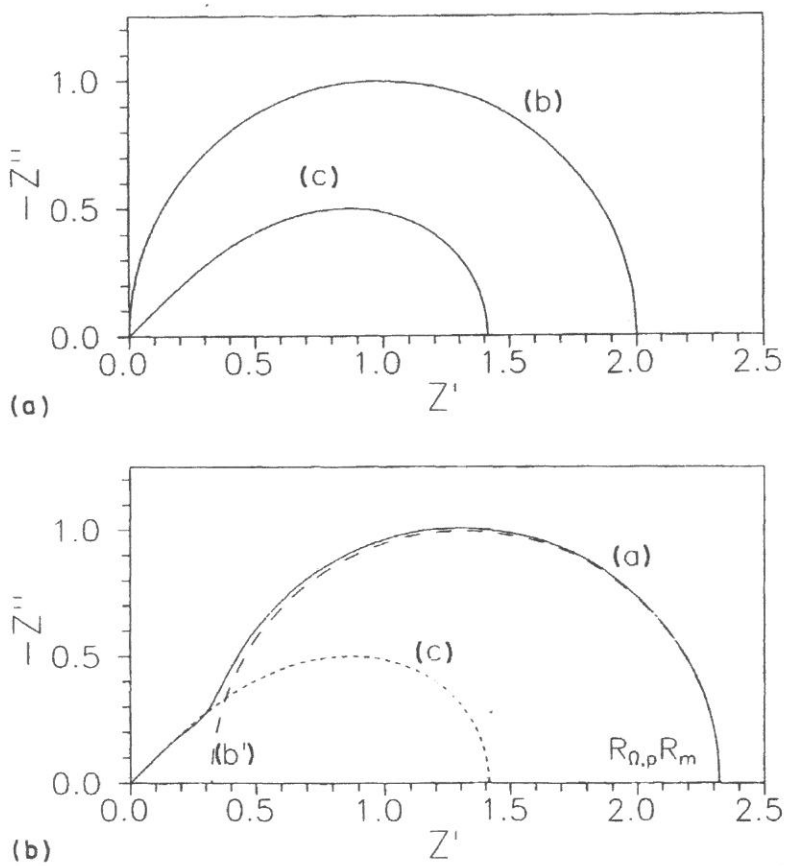

Fig. 2. Complex plane plots calculated for the porous electrode model: (a) general case, eqn. (18); (b) limiting case for shallow pores, eqn. (19); (c) limiting case for very deep pores, eqn. (20). Curve b′ is the same as curve b but shifted along the Z' axis. The parameters are $\mathscr{A}_p = 2$, $\mathscr{B}_p = 5$ s and $R_{\Omega,p} = 1\ \Omega\ \mathrm{cm}^2$.

In order to find the parameters of the semicircle in the general case, $\Lambda^{1/2}$ can be represented by the following equations:

$$\Lambda^{1/2} = x + \mathrm{j}y = (|\Lambda|)^{1/2}[\cos(\phi/2) + \mathrm{j}\sin(\phi/2)] \tag{21}$$

and $\phi = a\tan(\mathscr{A}_p\mathscr{B}_p\omega)$. Assuming $\omega \to \infty$, $y \to 0$ and $x \to (\mathscr{A}_p)^{-1/2}$, we obtain

$$\lim_{y\to 0}\{[\coth(x+\mathrm{j}y)]/(x+\mathrm{j}y)\} = (\mathrm{e}^{4x}-1)/[x(\mathrm{e}^{4x}-2\mathrm{e}^{2x}+1)]$$

$$= R_m = \mathscr{A}_p^{1/2}\coth(\mathscr{A}_p^{-1/2}) \tag{22}$$

Then the low-frequency limit $Z'(\omega \to 0) = R_s + R_{\Omega,p}R_m$. In Fig. 2, the semicircle b′ is shifted by $R_{\Omega,p}R_m - R_{ct}/s$ along the real axis.

Gassa et al. [20] considered the heterogeneity effects introduced by the porous cylindrical walls using the Cole–Cole dispersion formula and expressed Z_0 by the following equation:

$$Z_0 = R_{ct}\left[1 + (j\omega R_{ct}C_{dl})^{\phi}\right] \tag{23}$$

Their experimental results were fitted by means of five independent parameters: R_s, $R_{\Omega,p}$, $\mathscr{A}_p$, $\mathscr{B}_p$ and ϕ. However, as suggested by Lasia [42], it is more justifiable to use the CPE formula (eqn. (11)) to describe the impedance of the surface of the pore walls:

$$Z_0 = \left[1/R_{ct} + (j\omega)^{\phi}T\right]^{-1} \tag{24}$$

In this case the parameter $\Lambda = [1/\mathscr{A}_p + (j\omega)^{\phi}\mathscr{B}_p']$, where $\mathscr{B}_p' = T/a$. Cachet et al. [45] explained the roughness of their porous zinc electrode by introducing an empirical factor f into eqn. (16).

EXPERIMENTAL

Spiky filamentary nickel particles (Inco 255) were used to prepare the electrodes. The preparation method has been described in detail in previous papers [16–19]. A mixture of $La(H_2PO_4)_3$, $La(OH)_3$ and nickel powder was pressed under vacuum in a mold of diameter 1.3 cm. The LPBN nickel electrodes used in our studies contained 98 wt.% nickel. Nickel foil was added to the pellet produced in this way to ensure electrical contact. After preheating the pellets at 150°C for 12 h, polymerization was achieved by further heating at 300°C for 4–5 h under a flow of argon. One face and the sides of the electrodes were coated with Epofix resin (Struers) to obtain a (geometric) working surface area of 1.33 cm^2. According to the scanning electron micrographs of LPBN electrodes in ref. 16, it is possible to estimate the average pore size as approximately a few micrometers. However, scanning tunnelling micrographs also show the presence of shallow valleys 80 nm deep in the nickel powder [48].

Solutions were prepared using Barnstead Nanopure water of resistance 17.5 MΩ cm and NaOH solutions (Aldrich, semiconductor grade, 99.99%). No iron was detected in either the 30 wt.% solution or on the electrode surface after measurement using the induced coupled plasma–atomic emission spectroscopy (ICP-AES) and EDX methods. A polysulfone electrochemical cell [23–25,49] was used; the nickel grid counter-electrode had a geometric surface area of 40 cm^2 and the external Hg/HgO/1 M KOH reference electrode was immersed in a 30 wt.% NaOH solution maintained at room temperature. The experimentally determined reversible potential for the HER was time independent and was equal to −0.963 V. The same system was used for steady-state and ac impedance measurements. The ac measurements were carried out after approximately 40 cycles, each cycle comprising 30 min of galvanostatic electrolysis at 125 mA cm^{-2} and 10 min of Tafel curve measurements at cathodic current densities ranging from 0.1 μA cm^{-2}

to 250 mA cm^{-2}. After this treatment, all Tafel parameters became constant and reproducible ac results were obtained. The electrode potentials were corrected for the ohmic drop, which was determined by the current interruption and ac impedance techniques, both yielding similar results. The measurements were made using a PAR 273 galvanostat–potentiostat and an EG&G 5208 lock-in analyzer controlled by a Commodore PC 10-III microcomputer.

The ac measuring procedures were similar to those used in refs. 13–17, 21 and 32, where the ac amplitude was 10 mV peak-to-peak. The real and imaginary components of the complex plane plots were analyzed using a modified version of the complex non-linear least-squares fitting program (CNLS) of Macdonald et al. [50], from which the experimental parameters were determined. The approximations of the ac results were achieved using various models (Figs. 1(a)–(e)). Details of the calculation procedures are given with the experimental results.

The mechanism of the HER was determined from the dependences of both the parameter $A = 1/R_{ct}$ (Fig. 1(e)) and the current density j on the overpotential η. The rate constants were evaluated using the non-linear least-squares (NLS) method [13–17,21,32].

RESULTS

Steady-state measurements

Several studies of HER steady-state measurements in alkaline solutions have been reported in the literature [19–26,28,29,51]: the electrolyte concentrations used in these studies reached 26 M and temperatures ranged from 20 to 200°C. The general conclusion to be drawn from the results is that the polarization characteristics are almost independent of the NaOH concentration for flat electrodes made of different metals [8,25,26,29]. Typical values of the Tafel parameters are given in Table 1: the Tafel slopes and exchange current densities in 30 wt.% alkaline solutions at 70°C are about 150 mV and 5×10^{-5} A cm^{-2} respectively. In the present investigation, Tafel behavior was observed for hydrogen overpotentials ranging from -80 to -300 mV. As can be seen in Table 1 for tests 1, 6 and 7 and updated in other papers [6,9,52–54], deactivation of the nickel electrodes occurs in hot concentrated alkaline electrolytes even when iron and heavy metals are not detected either in the solution or on the cathode surface after electrolysis. Our electrolyte was free from iron and heavy metal impurities; the LPBN electrode was deactivated and after ca. 10 h of galvanostatic multicycle testing, as described above, stable Tafel parameters were obtained. It should be added that the potential of the LPBN cathode at zero current is shifted in the negative direction by approximately 30 mV and deactivation is characterized by the change in the overpotential at 250 mA cm^{-2} from an initial value of -200 mV to -294 mV after ca. 10 h of measurement. At the same time, the Tafel slope changes from 167 mV/decade to 158 mV/decade.

TABLE 1

Kinetic parameters of the hydrogen evolution reaction on nickel cathodes in concentrated alkaline solutions

Test no.	Solution	b/mV	j_0/mA cm^{-2}	Conditions	Reference
1	30 wt.% NaOH, 70°C	167 158	7 3	After 2 h and after 18 h of multicycle experiment	This work
2	34 wt.% KOH, 70°C	155 155	0.01 0.25	Smooth Ni, Sintered Ni $j \geqslant 0.1$ A cm^{-2}	50
3	30 wt.% NaOH, 75°C	144 141	0.06 0.12	Smooth Ni Rough Ni	25, 26
4	30 wt.% NaOH 50°C 100°C	 137 161	 0.34 1.6	Smooth Ni, hydrogen pressure 2.1 MPa	8
5	30 wt.% KOH, 70°C	104	0.07	Smooth Ni, solution contains 5 ppm Fe	23
6	30 wt.% KOH, 70°C	99 156	0.055 0.085	Smooth Ni after 1 min After 40 days under cathodic polarization, solution contains 5 ppm Fe	24
7	30 wt.% KOH, 37°C	100 300	0.002 0.1	Smooth Ni after 1 min After ca. 3 h under cathodic polarization	11

Other workers investigating the influence of porosity on the Tafel parameters [25,26,50] have reported no difference between flat and rough electrodes as far as the Tafel slopes are concerned (Table 1, tests 2 and 3). However, an increase in the surface area is evident as the roughness factor increases, resulting in a higher exchange current density. Brown et al. [25,26] claimed that, in general, the difference in behavior between rough and smooth electrodes depends on the sodium hydroxide concentration and temperature. They found [26] that the Tafel slope measured under the same experimental conditions is smaller for rough electrodes than for smooth ones made of the same metal. The difference is even more significant for a rougher electrode at a higher temperature and in a very concentrated electrolyte [26]. It is worth noticing that the trend of these experimental changes contradicts the predictions of de Levie [39] and Tilak et al. [55], i.e.

the Tafel slope b for porous electrodes should be twice that for a smooth cathode. Mulder et al. [40] have shown that the Tafel slope for fractal electrodes is generally larger and equal to b/ϕ, where ϕ is the CPE exponent. Low Tafel slopes of 76 mV/decade were observed, for example, on porous electrodes coated with Raney nickel and with Raney nickel + cobalt in 30 wt.% NaOH at 70°C [19]. However, the same parameter for electrodes made of nickel and Raney nickel pressed powders is 146 mV/decade [14]. The present discussion leads to the conclusion that a mechanistic interpretation of HER studies on porous and rough electrodes based only on steady-state results is highly questionable [25,26].

Ac impedance

The plots of the experimental complex impedance Z'' vs. Z' and of Z'' vs. the logarithm of the angular frequency are shown in Fig. 3. The ac measurements were performed on LPBN electrodes at different applied overpotentials in 30 wt.% sodium hydroxide solution at 70°C in the overpotential range from -80 to -204 mV. As seen in the figure, the ac data were obtained in the linear region of the Tafel plot. Assumption of the steady state is fulfilled in this potential range and the kinetic parameters of the HER can be calculated. The shape of the experimental complex plane impedance plots is typical of porous electrodes [27,39,44–47,56]. Since the penetration depth λ of the ac signal depends on frequency, at higher frequencies the pores behave as if they were semi-infinite and a linear part of the Nyquist graph is observed with a phase angle of 45°. An analogous performance is predicted by de Levie, even for a pure capacitance system [40,43,44]. Our measurements were performed at frequencies down to 0.1 Hz because of the influence of the HER at lower frequencies. At the lowest frequencies used, the pores respond like a flat electrode. The R_{ct} values calculated using the CPE model from the semicircles obtained at lower frequencies (Figs. 3(a) and 3(b)) are approximately equal to the charge-transfer resistance of the HER.

Figures 3(a)–3(g) show the experimental complex plane, Z' vs. log ω and Z'' vs. log ω impedance plots fitted to various models. The experimental data agree very well with the de Levie porous model modified according to eqn. (24). The real and imaginary components Z' and Z'' obtained for all frequencies at various dc potentials were analyzed using the CNLS program [50] and modified in order to find the experimental values of parameters $\mathscr{A}_p$, $\mathscr{B}'_p$, R_s, $R_{\Omega,p}$ and ϕ. All these parameters were defined earlier and their values are presented in Table 2. The values of phase angles ϕ are mostly close to unity, which suggests that the LPBN electrode can be fitted to the porous model in which the impedance of the pore walls resembles that of a flat surface. In fact, assuming $\phi = 1$, the fit obtained is only slightly worse than that with ϕ as an adjustable parameter. It should be noted that, according to Gassa et al. [20], the Tafel slope b of the cathodic reaction can be calculated from the ac impedance results using the equation $b = -(\partial\eta/\partial \log \mathscr{A}_p)$. This value equals 143 mV/decade and is close to that yielded by the steady-state measurements, i.e. 158 mV/decade. The fact that the two methods

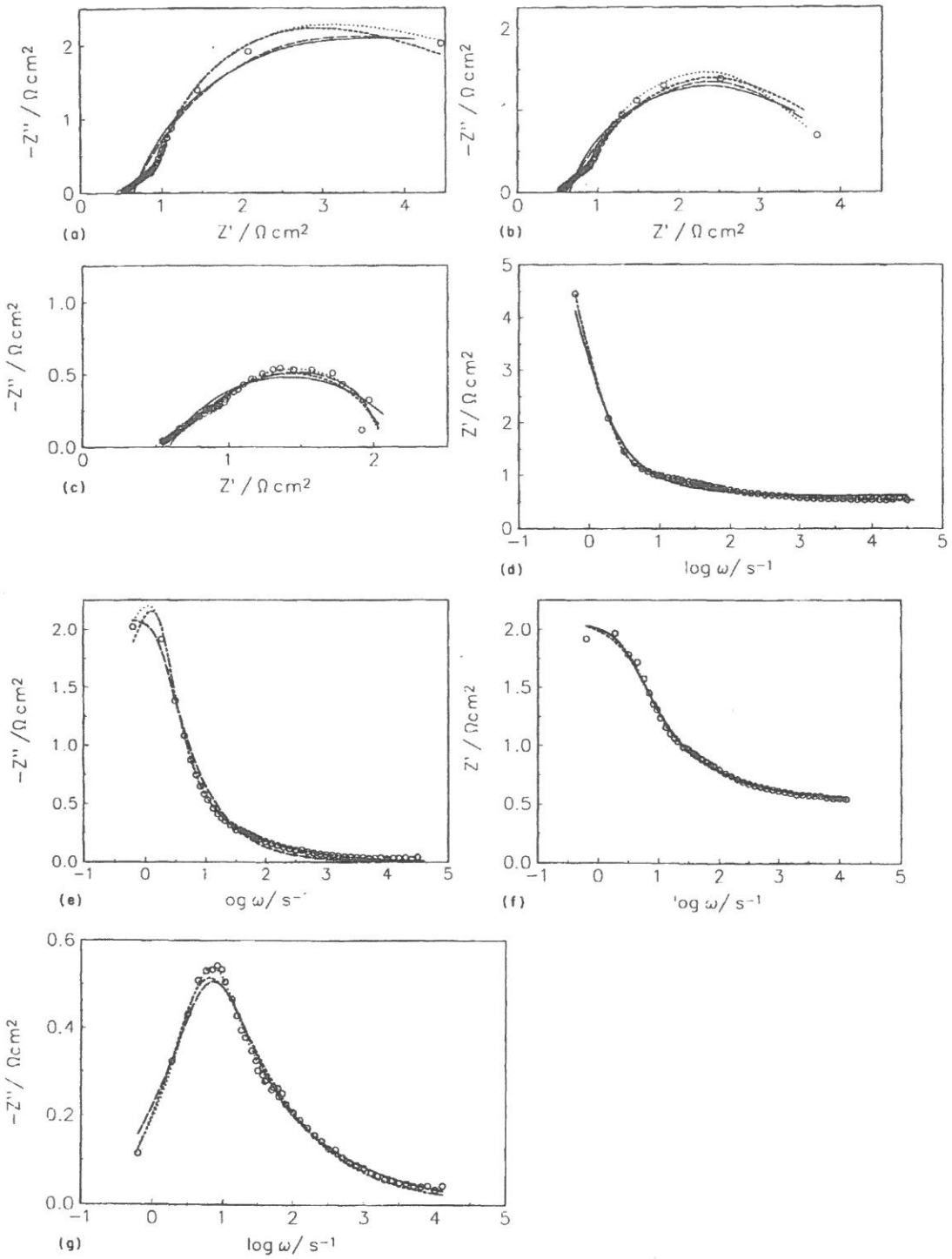

Fig. 3. Experimental (symbols) and simulated (lines) complex plane and $Z - \log w$ plots for LPBN electrodes in 30 wt.% NaOH at 70°C and the following values of η: (a) −80 mV; (b) −127 mV; (c) −175 mV; (d) −80 mV; (e) −80 mV; (f) −175 mV; (g) −175 mV. The following models were used: ····· porous; - - - - - - CPE1-CPE; — — — fractal; ——— CPE.

TABLE 2

Parameter values and their standard deviations obtained using the porous electrode model to approximate experimental ac impedance diagrams for a LPBN electrode in 30 wt.% NaOH at 70°C

η/mV	$\mathscr{A}_p$	$\mathscr{B}'_p/s^{\phi}$	ϕ	$R_{\Omega,p}/\Omega\ cm^2$
−80	3.56 ±0.08	0.265±0.005	0.997±0.004	1.32±0.02
−105	2.95 ±0.05	0.249±0.003	0.978±0.003	1.32±0.02
−127	2.07 ±0.08	0.231±0.01	1.006±0.009	1.38±0.04
−143	1.55 ±0.04	0.206±0.006	0.975±0.006	1.34±0.03
−159	1.32 ±0.08	0.172±0.012	0.924±0.013	1.22±0.05
−168	1.01 ±0.04	0.178±0.009	0.944±0.009	1.28±0.04
−175	0.906±0.04	0.171±0.01	0.940±0.010	1.24±0.04
−182	0.805±0.04	0.175±0.01	0.912±0.010	1.26±0.05
−190	0.750±0.05	0.167±0.02	0.877±0.010	1.25±0.06
−204	0.550±0.08	0.157±0.03	0.894±0.020	1.22±0.12

For all overpotentials R_s was approximately equal to 0.50 $\Omega\ cm^2$.

give approximately the same value for the Tafel slope is not surprising. As can be seen in Fig. 2, at low frequencies a semicircle develops which corresponds to the flat electrode case (eqn. (19), $l \ll \lambda$), and the same model should be used to describe the steady-state experiments instead of those derived for porous [43,55] or fractal [38–40] electrodes. The values of the capacitance parameters $\mathscr{B}'_p$ are almost constant for overpotentials higher than −150 mV. It should also be noted that the porous model provides an opportunity of determining parameters $R_{ct} = R_{\Omega,p}\mathscr{A}_p$ and $T = \mathscr{B}'_p/R_{\Omega,p}$ which are presented in Table 4 below.

The CPE and fractal models were also used to fit the experimental ac impedance data. As can be seen in Fig. 2, the model containing one CPE (Fig. 1(b)) cannot be used to describe the experimental data over the entire frequency range. However, the fractal model fits the experimental complex plane impedance diagrams very well for overpotentials higher than −125 mV. In this case, as mentioned in the Introduction, the phase angle values are approximately equal to 45°.

A very good fit to the experimental data was also obtained using the equivalent circuit containing two CPEs presented in Fig. 1(e). This model has previously been used to approximate the complex plane plots obtained in nickel + zinc powder electrodes, and the diameter of the first semicircle did not change with overpotential [57]. Two sets of parameters—A_1, T_1 and ϕ_1 for the first flat part of the impedance diagram and $A = 1/R_{ct}$, T and ϕ for the second part (faradaic process), were fitted to the data (Table 3). The approximation was performed by first fitting experimental data for the second semicircle and then, having fixed ϕ, determining parameters A_1, T_1, ϕ_1, A and T for all points on the experimental complex plane diagram. Similar results were obtained when all six parameters were assumed to be adjustable, the only difference being that the value of ϕ was closer to unity. This model is based on the fact (theoretical part) that the second semicircle, which corresponds to the parallel connection of the HER charge-transfer resistance and the double-layer capacitance, is not affected by the pore texture

TABLE 3

Parameter values and their standard deviations obtained using the CPE1-CPE equivalent circuit model to approximate experimental ac impedance diagrams for a LPBN electrode in 30 wt.% NaOH at 70°C

η/mV	A_1/Ω^{-1} cm^{-2}	T_1/F cm^{-2} s$^{\phi-1}$	ϕ_1	$C_{dl,1}$/F cm^{-2}
−80	2.10±0.11	0.181±0.023	0.584±0.020	0.020
−105	1.75±0.10	0.219±0.022	0.531±0.015	0.018
−127	1.36±0.24	0.344±0.063	0.434±0.028	0.017
−143	1.19±0.21	0.310±0.056	0.436±0.028	0.015
−159	1.93±0.25	0.206±0.039	0.521±0.029	0.014
−168	1.85±0.46	0.365±0.097	0.415±0.038	0.021
−175	1.85±0.31	0.239±0.052	0.471±0.033	0.011
−182	1.87±0.20	0.162±0.025	0.560±0.025	0.014
−190	1.72±0.26	0.307±0.053	0.426±0.024	0.011
−204	2.40±0.32	0.163±0.032	0.545±0.028	0.011
η/mV	A/Ω^{-1} cm^{-2}	T/F cm^{-2} s$^{\phi-1}$	ϕ	C_{dl}/F cm^{-2}
−80	0.166±0.009	0.216±0.005	0.935±0.007	0.185
−105	0.238±0.007	0.213±0.005	0.944±0.006	0.186
−127	0.341±0.012	0.208±0.011	0.924±0.007	0.170
−143	0.519±0.024	0.198±0.013	0.938±0.011	0.168
−159	0.613±0.022	0.197±0.012	0.859±0.016	0.130
−168	0.699±0.044	0.209±0.016	0.787±0.016	0.105
−175	0.938±0.057	0.180±0.014	0.867±0.016	0.117
−182	1.097±0.050	0.204±0.014	0.893±0.010	0.148
−190	1.196±0.083	0.201±0.014	0.819±0.013	0.110
−204	1.535±0.111	0.178±0.016	0.837±0.018	0.100

For all overpotentials R_s was approximately equal to 0.50 Ω cm^2. Parameter ϕ_2 was calculated from the second semicircle (details in text).

[27,43]. The values of ϕ presented in Table 3 are approximately equal to 0.9 in most cases, very similar to those found using the porous model (Table 2). It should be stressed that in the present work ϕ is considered as an empirical parameter describing all kinds of inhomogeneities, i.e. physical, chemical and geometrical [13,43]. In the case of the LPBN electrode, two factors can cause pore "roughening": geometrical, i.e. the presence of valleys 80 nm deep on nickel powder particles [48], and chemical, i.e. the appearance of nickel oxides (hydroxides) on the electrode surface. These hydroxides are assumed to be non-reducible during the HER [25,58,59].

The double-layer capacitance values (Table 3) were calculated using eqn. (13). The double-layer capacitance can be used to estimate the roughness factor $\mathscr{R}$, as being equal to the experimental capacitance of the double layer divided by that of smooth metal and assumed to be approximately equal to 20 μF cm^{-2} [60]. The roughness factor for the LPBN electrode in 30 wt.% NaOH at 70°C is approximately 5000, which is slightly higher than the value of 4400 established by the Brunauer–Emmett–Teller (BET) method [17] and is five times higher than that obtained in 1 M NaOH at 25°C [16].

TABLE 4

Comparison of parameters obtained from the porous electrode and CPE1-CPE models

η/mV	$R_{ct} = \mathscr{A}_p R_{\Omega,p}$ */Ω cm^2	$T = \mathscr{B}_p / R_{\Omega,p}$ */ F cm^{-2} s$^{\phi-1}$	C_{dl} */F cm^{-2}	$R_{ct} = 1/A$ **/ Ω cm^2
−80	4.699	0.201	0.199	6.024
−105	3.894	0.189	0.179	4.202
−127	2.857	0.167	0.170	2.932
−143	2.077	0.154	0.144	1.927
−159	1.610	0.141	0.111	1.631
−168	1.293	0.139	0.117	1.431
−175	1.123	0.138	0.114	1.066
−182	1.014	0.139	0.104	0.912
−190	0.938	0.134	0.087	0.836
−204	0.671	0.129	0.087	0.652

* From porous electrode model.
** From CPE1-CPE model.

From the data presented in Table 4, it can be concluded that the porous electrode model and the CPE1-CPE model give similar results as far as charge-transfer resistances and double-layer capacities are concerned. The difference in the double-layer capacities calculated from the two models is lower than 30% over the whole range of overpotentials. Moreover, the difference between charge-transfer resistances is no higher than 10% for the two models, with the overpotentials being higher than −80 mV. This fact can be understood by comparing the CPE1-CPE and porous electrode models (Fig. 2). The semicircle formed at low frequencies (Fig. 2, curve a) yields a larger radius R_{ct} than that corresponding to the semicircle formed on a flat electrode (Fig. 2, curve b′).

An approximation of the dependences $A = 1/R_{ct}$ vs. η and j vs. η was carried out by adjusting the rate constants k_1, k_{-1} and k_2 and transfer coefficients α_1 and α_2 by the NLS method. The best approximation of the experimental data was obtained by assuming the Volmer–Heyrovsky mechanism. The results are presented in Figs. 4 and 5. The kinetic parameters of the HER that were found on the basis of this procedure are presented in Table 5. The values of rate constants k_1 and k_2 are very similar, which indicates mixed control of the HER by the Volmer and Heyrovsky reactions. On the basis of the values of kinetic parameters k_1 and j_0 (exchange current density) divided by the roughness factor $\mathscr{R}$, the intrinsic

TABLE 5

Kinetic parameters of the HER and their standard deviations obtained from ac impedance and steady-state polarization measurements for a LPBN electrode in 30 wt.% NaOH at 70°C

Model	$10^8 k_1$ / mol cm^{-2} s^{-1}	$10^8 k_{-1}$ / mol cm^{-2} s^{-1}	$10^8 k_2$ / mol cm^{-2} s^{-1}	α_1	α_2
CPE1-CPE	1.48 ± 0.43	0.84 ± 3.09	2.68 ± 0.44	0.795 ± 0.028	0.382 ± 0.017
Porous	2.53 ± 1.26	0.89 ± 2.12	2.31 ± 0.33	0.765 ± 0.019	0.397 ± 0.014

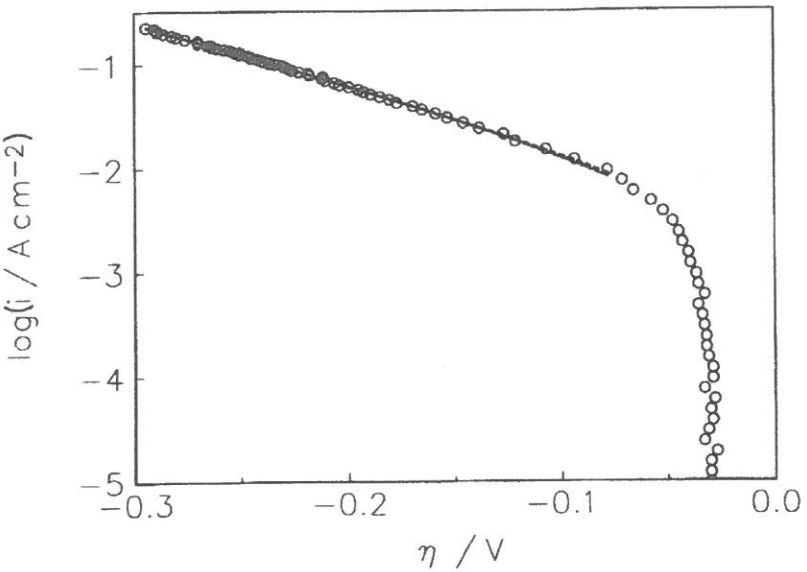

Fig. 4. Experimental (symbols) Tafel plot and that calculated using the kinetic parameters from Table 3 (———) and Table 4 (— — —) obtained on a LPBN electrode in 30 wt.% NaOH at 70°C.

electrocatalytic activity of the electrode can be estimated. The following values were found for the LPBN electrode in 30 wt.% NaOH at 70°C: $k_1/\mathscr{R} = 3 \times 10^{-12}$ mol cm^{-2} s^{-1} and $j_0/\mathscr{R} = 1.4 \times 10^{-6}$ A cm^{-2} (after 2 h of electrolysis) for the LPBN electrode in 30 wt.% NaOH at 70°C. The two values are very close to

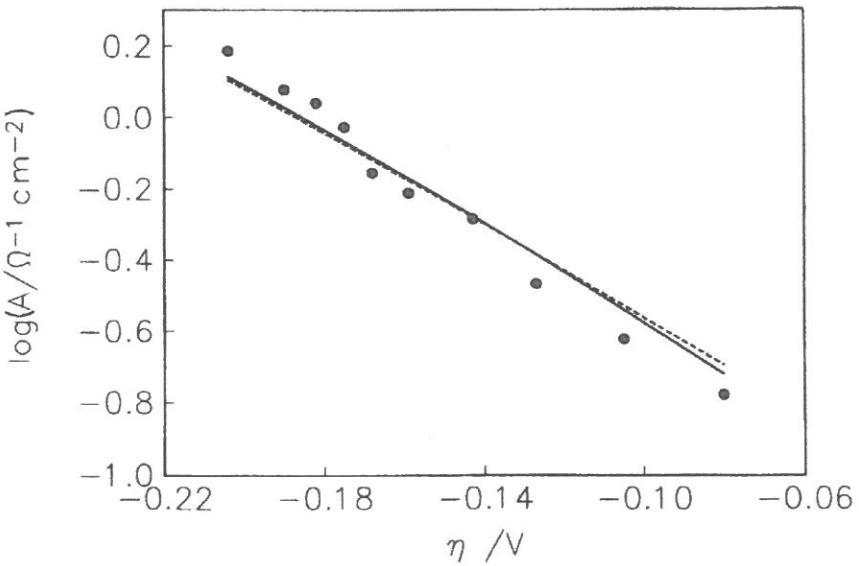

Fig. 5. Dependence of the experimental (symbols) and calculated values of the logarithm of parameters A from Table 3 (———) and Table 4 (— — —) on the overpotential for a LPBN electrode in 30 wt.% NaOH at 70°C.

$k_1 = 4 \times 10^{-12}$ mol cm^{-2} s^{-1} and $j_0 = 1.8 \times 10^{-6}$ A cm^{-2}, which were established earlier [61] for the polycrystalline nickel electrode in 1 M NaOH at 25°C. Nevertheless, the value of $k_1/\mathscr{R}$ obtained for the LPBN electrode in 1 M NaOH at 25°C is approximately an order of magnitude higher than that for the electrode polymerized at 300°C, and only three times larger than $k_1/\mathscr{R}$ for the LPBN electrode polymerized at 600°C when significant destruction of the nickel powder fractal structure was observed [16]. It should be noted that rate constants and transfer coefficients presented in Table 5 and calculated using parameters A from the two CPE model or $A = 1/\mathscr{A}_p R_{\Omega,p}$ from the porous electrode model (Table 4) are very close. The calculated dependence of the logarithms of both the current density (Fig. 4) and the A parameters (Fig. 5) on the overpotential is also very similar. The calculations using experimentally determined rate constants show that the term $B/(j\omega + C)$ is negligible and the intrinsic impedance is adequately represented by a single resistance $1/A$.

Since the physical sense of the parameters CPE_1 and A_1 related to the first semicircles is not clear, the values of A_1, T_1 and ϕ_1 in Table 3 are not discussed here. It is possible that the straight line obtained at high frequency is a particular case of a more general model which may produce two semicircles, as in the case of nickel + zinc [57] and, recently, nickel + aluminum pressed powder electrodes.

CONCLUSIONS

The HER was studied on LPBN electrodes in a 30 wt.% NaOH solution at 70°C by the ac impedance and steady-state techniques. Approximation of the experimental complex plane impedance diagrams was performed successfully using two models: de Levie's porous electrode model [43], modified to take into account the heterogeneity of the pore [20,42], and the circuit containing the two CPEs (Fig. 1(e)) [57]. The disadvantage of the first model is that in the deep pore limit ($\lambda \ll l$) it includes specific pore parameters which in many cases are not easy to determine. However, in general the kinetic parameters of the HER and C_{dl} can be obtained. On the basis of these models, it was established that the HER proceeds via the Volmer–Heyrovsky reaction with mixed rate control. It was also concluded that the intrinsic electrocatalytic activity of the LPBN electrode in 30 wt.% NaOH at 70°C is similar to that of the polycrystalline nickel electrode and lower than that found for a LPBN electrode in 1 M NaOH at 25°C. Since the influence of inhomogeneity and/or porosity of the electrode on the Tafel parameters is a complex function of the experimental conditions, the steady-state method cannot be used alone to evaluate the kinetics and mechanism of the electrochemical process.

ACKNOWLEDGEMENTS

The financial support from NSERC (Strategic Grant) and the Ministère de l'Energie et des Ressources du Québec (Chair sur l'hydrogène) is gratefully acknowledged.

established
H at 25°C.
1 M NaOH
e electrode
the LPBN
kel powder
nstants and
ers A from
el (Table 4)
the current
is also very
ts show that
adequately

to the first
ot discussed
a particular
1 the case of
ectrodes.

ıtion at 70°C
f the experi-
lly using two
account the
CPEs (Fig.
limit ($\lambda \ll l$)
o determine.
be obtained.
ceeds via the
ncluded that
.% NaOH at
wer than that
influence of
rameters is a
ethod cannot
ectrochemical

Ministère de
is gratefully

REFERENCES

1 S. Trasatti, Adv. Electrochem. Sci. Eng., 2 (1992) 2.
2 S. Dutta, Int. J. Hydrogen Energy, 15 (1990) 379.
3 G.A. Crawford and S. Benzimra, Int. J. Hydrogen Energy, 11 (1986) 691.
4 L.J. Vracar and B.E. Conway, Int. J. Hydrogen Energy, 15 (1990) 701.
5 B.V. Tilak, A.C. Ramamurthy and B.E. Conway, Proc. Indian Acad. Sci. (Chem. Sci.), 97 (1986) 359.
6 L. Brossard, Int. J. Hydrogen Energy, 16 (1991) 13.
7 J. Divisek, J. Mergel and H. Schmitz, Int. J. Hydrogen Energy, 15 (1990) 105.
8 Y. Ogata, H. Hori, M. Yasuda and F. Hine, J. Electrochem. Soc., 135 (1988) 76.
9 J.-Y. Huot, J. Electrochem. Soc., 136 (1989) 1933.
10 G. Fiori and C. Mari, Int. J. Hydrogen Energy, 12 (1987) 159.
11 H.E.G. Rommal and P.J. Moran, J. Electrochem. Soc., 132 (1985) 325.
12 C. Iwakura, N. Furukawa and M. Tanaka, Electrochim. Acta, 37 (1992) 757.
13 P. Los and A. Lasia, J. Electroanal. Chem., 333 (1992) 115.
14 P. Los, A. Rami and A. Lasia, J. Appl. Electrochem., 23 (1993) 135.
15 L. Chen and A. Lasia, J. Electrochem. Soc., 138 (1991) 3321.
16 H. Dumont, P. Los, L. Brossard, A. Lasia and H. Ménard, J. Electrochem. Soc., 139 (1992) 2143.
17 H. Dumont, P. Los, L. Brossard, A. Lasia and H. Ménard, J. Appl. Electrochem., in press.
18 H. Dumont, P.K. Wrona, L. Brossard, J.M. Lalancette and H. Ménard, J. Appl. Electrochem., 22 (1992) 1049.
19 Y. Choquette, H. Ménard and L. Brossard, Int. J. Hydrogen Energy, 15 (1990) 21.
20 L.M. Gassa, J.R. Vilche, M. Ebert, K. Juttner and W.J. Lorenz, J. Appl. Electrochem., 20 (1990) 677.
21 Y. Choquette, L. Brossard, A. Lasia and H. Ménard, Electrochim. Acta, 35 (1990) 1251.
22 T. Kenjo, J. Electrochem. Soc., 133 (1986) 2051.
23 J.-Y. Huot, J. Electrochem. Soc., 136 (1989) 1933.
24 J.-Y. Huot and L. Brossard, Int. J. Hydrogen Energy, 12 (1987) 821.
25 A.P. Brown, M. Krumpelt, R.O. Loutfy and N.P. Yao, J. Electrochem. Soc., 129 (1982) 2481.
26 A.P. Brown, M. Krumpelt, R.O. Loufty and N.P. Yao, Electrochim. Acta, 27 (1982) 557.
27 J.-P. Candy, P. Fouilloux, M. Keddam and H. Takenouti, Electrochim. Acta, 27 (1982) 1585.
28 T.S. Lee, J. Electrochem. Soc., 122 (1975) 171.
29 T.S. Lee, J. Electrochem. Soc., 118 (1971) 1278.
30 D.A. Harrington and B.E. Conway, J. Electroanal. Chem., 221 (1987) 1.
31 D.A. Harrington and B.E. Conway, Electrochim. Acta, 32 (1987) 1703.
32 A. Lasia and A. Rami, J. Electroanal. Chem., 294 (1990) 123.
33 B.G. Pound, R.P. Singh and D.D. Macdonald, J. Power Sources, 18 (1986) 1.
34 J. Balej, Int. J. Hydrogen Energy, 16 (1991) 353.
35 J. Balej, Int. J. Hydrogen Energy, 10 (1985) 365.
36 J. Balej, Int. J. Hydrogen Energy, 10 (1985) 233.
37 G.J. Brug, A.L.G. Van der Eeden, M. Sluyters-Rehbach and J.H. Sluyters, J. Electroanal. Chem., 176 (1984) 275.
38 R. de Levie, J. Electroanal. Chem., 261 (1989) 1.
39 R. de Levie, J. Electroanal. Chem., 281 (1990) 1.
40 W.H. Mulder, J.H. Sluyters, T. Pajkossy and L. Nyikos, J. Electroanal. Chem., 285 (1990) 103.
41 L. Chen and A. Lasia, J. Electrochem. Soc., 139 (1992) 3458.
42 A. Lasia, Int. J. Hydrogen Energy, in press.
43 R. de Levie, Electrochem. Electrochem. Eng., 6 (1967) 329.
44 C. Cachet and R. Wiart, J. Electroanal. Chem., 195 (1985) 21.
45 C. Cachet, C.P. Pauli and R. Wiart, Electrochim. Acta, 30 (1985) 719.
46 C. Cachet and R. Wiart, Electrochim. Acta, 29 (1984) 145.
47 J.-P. Candy, P. Fouilloux, M. Keddam and H. Takenouti, Electrochim. Acta, 26 (1981) 1029.
48 B.A. Kwetkus and K. Sattler, Surf. Sci., 275 (1992) 201.

49 Y. Choquette, L. Brossard and H. Ménard, Int. J. Hydrogen Energy, 15 (1990) 551.
50 J.R. Macdonald, J. Schoonman and A.P. Lehner, J. Electroanal. Chem., 131 (1982) 77.
51 A.J. Appleby, G. Crépy and J. Jacquelin, Int. J. Hydrogen Energy, 3 (1978) 21.
52 D.M. Soares, O. Teschke and I. Torriani, J. Electrochem. Soc., 139 (1992) 98.
53 M.A. Riley and P.J. Moran, J. Electrochem. Soc., 133 (1986) 760.
54 L. Brossard and J.-Y. Huot, J. Appl. Chem., 19 (1989) 882.
55 B.V. Tilak, S. Venkatesh and S.K. Rangarajan, J. Electrochem. Soc., 136 (1989) 1977.
56 I.D. Raidstrick, Electrochim. Acta, 35 (1990) 1579.
57 L. Chen and A. Lasia, J. Electrochem. Soc., 139 (1992) 3214.
58 W. Visscher and E. Barendrecht, J. Appl. Electrochem., 10 (1980) 269.
59 Y. Jin Kim, S. Srinivasan and A.J. Appleby, J. Appl. Electrochem., 20 (1990) 377.
60 S. Trasatti and O.A. Petrii, Pure Appl. Chem., 63 (1991) 711.
61 A. Lasia and A. Rami, J. Electroanal. Chem., 294 (1990) 123.